Remotely Triggered Assembly of 3D Mesostructures Through Shape-Memory Effects

Jun Kyu Park, Kewang Nan, Haiwen Luan, Ning Zheng, Shiwei Zhao, Hang Zhang, Xu Cheng, Heling Wang, Kan Li, Tao Xie, Yonggang Huang, Yihui Zhang,* Seok Kim,* and John A. Rogers*

3D structures that incorporate high-performance electronic materials and allow for remote, on-demand 3D shape reconfiguration are of interest for applications that range from ingestible medical devices and microrobotics to tunable optoelectronics. Here, materials and design approaches are introduced for assembly of such systems via controlled mechanical buckling of 2D precursors built on shape-memory polymer (SMP) substrates. The temporary shape fixing and recovery of SMPs, governed by thermomechanical loading, provide deterministic control over the assembly and reconfiguration processes, including a range of mechanical manipulations facilitated by the elastic and highly stretchable properties of the materials. Experimental demonstrations include 3D mesostructures of various geometries and length scales, as well as 3D aquatic platforms that can change trajectories and release small objects on demand. The results create many opportunities for advanced, programmable 3D microsystem technologies.

3D mesostructures are of growing interest due to their potential to create engineering design options that are unavailable in conventional 2D counterparts, with relevance in areas ranging from radio-frequency communications,[1–5] to sensors and actuators,[6–11] to energy harvesters,[12–16] and to biomedical devices.[17–20] Fabrication techniques such as 3D printing,[2,9,20–22] templated growth,[23–25] colloidal self-assembly,[26–28] and controlled folding/rolling[16,29–31] offer various interesting capabilities[32–37] in this context. Emerging approaches based on the compressive buckling of patterned thin-film precursors into deterministic 3D geometries[3–6,11,12,15,18,38,39] are attractive due to their compatibility with established

J. K. Park, Dr. K. Nan, Prof. S. Kim
Department of Mechanical Sciences and Engineering
University of Illinois at Urbana-Champaign
Urbana, IL 61801, USA
E-mail: skm@illinois.edu
Dr. K. Nan
Department of Bioengineering
Harvard University
Cambridge, MA 02138, USA
Dr. H. Luan, Prof. Y. Huang
Center for Bio-Integrated Electronics
Department of Mechanical Engineering
Department of Civil and Environmental Engineering
Department of Materials Science and Engineering
Northwestern University
Evanston, IL 60208, USA
Dr. N. Zheng, Prof. T. Xie
State Key Laboratory of Chemical Engineering
College of Chemical and Biological Engineering
Zhejiang University
Hangzhou 310027, P. R. China
S. Zhao, Dr. H. Wang, Dr. K. Li
Department of Mechanical Engineering
Department of Civil and Environmental Engineering
Department of Materials Science and Engineering
Northwestern University
Evanston, IL 60208, USA

S. Zhao
School of Aeronautic Science and Engineering
Beihang University
Beijing 100191, P. R. China
H. Zhang, X. Cheng, Prof. Y. Zhang
Applied Mechanics Laboratory
Department of Engineering Mechanics
Center for Flexible Electronics Technology
Tsinghua University
Beijing 100084, P. R. China
E-mail: yihuizhang@mail.tsinghua.edu.cn
Dr. K. Li
Department of Engineering
University of Cambridge
Cambridge CB2 1PZ, UK
Prof. J. A. Rogers
Departments of Materials Science and Engineering
Biomedical Engineering
Neurological Surgery, Chemistry, Mechanical Engineering
Electrical Engineering and Computer Science
Simpson Querrey Institute and Feinberg Medical School
Center for Bio-Integrated Electronics
Northwestern University
Evanston, IL 60208, USA
E-mail: jrogers@northwestern.edu

monolithic microfabrication schemes, including material choices that encompass device-grade semiconductors, conductors, and insulators, with a broad range of feature sizes and geometries, via high-throughput batch processing. Here, thin-film precursors fabricated by conventional microfabrication techniques and transferred onto prestrained elastomeric substrates transform into 3D architectures upon release of this prestrain.

The current version of this scheme supports many design and functional options, but it does not, however, afford an ability to initiate 3D structure formation or shape reconfiguration remotely, in an on-demand fashion. Consequently, the capabilities do not address requirements for deployment in enclosed or delicate environments such as those encountered in biology or for programmed, automated shape transformations such as in microrobotics.[16,40] Shape-memory effects in certain classes of polymers and metals might offer relevant utility in this context.[41–44] Recent work shows, in fact, that 2D precursors of shape-memory polymers (SMPs) provide routes to free-standing 3D mesostructures by temporary shape fixing.[3] Extensions of these concepts have the potential to allow for triggered assembly, when implemented with SMP materials that offer a suitable collection of mechanical stiffnesses, levels of stretchability, and transition temperatures, in specific design and fabrication schemes.[45–48]

This paper presents a class of multifunctional SMPs with the key required thermomechanical properties, along with a set of processing strategies that serve as a platform for remote, on-demand formation of 3D mesostructures via coupled thermal/mechanical actuation. The SMPs also enable controlled changes in geometry through temporary shape fixing. Demonstrations include a 3D aquatic structure that can change motion trajectories and release small objects, on-demand. The results add to the growing collection of capabilities in 3D microsystems, with potential relevance in ingestible medicines, microrobots, and tunable optoelectronics.

Important properties of SMPs for purposes presented here, particularly for biomedical applications, include the following: I) low elastic modulus and large stretchability in the rubbery state; II) a transition temperature similar to human body temperature; III) chemical biocompatibility; and IV) ability to structure into large, thin films and patterns.

The most widely used SMPs in flexible electronics are amorphous (e.g., epoxy and polystyrene) because of their excellent processability, high transparency, and tunable thermal transition temperatures.[3,49–51] Most demonstrations, however, rely on bending and twisting, without large levels of stretching. The findings reported here rely on semicrystalline SMPs with low modulus and high stretchability that result from a high molecular mass between crosslinkers required for crystallization, and corresponding low crosslinking density. **Figure 1**a illustrates the crystallization-enabled shape-memory mechanisms for shape fixing and recovery, by cooling below the crystallizing temperature (T_c) and heating above the melting temperature (T_m), respectively.

The SMP used here results from the reaction of polycaprolactone diol (PCL) with a crosslinker (poly(hexamethylene diisocyanate, PHDI)) and an extender (hexamethylene diisocyanate, HDI). Suitable formulations offer a T_m of 36.5 °C that is close

to body temperature, through appropriate selection of the molar ratio between the crosslinker and the extender. Figure S1a (Supporting Information) shows examples of changes in T_m for several molar ratios (1:0, 1:1, and 1:3). The resulting SMPs show a low rubbery-state modulus (0.82 ± 0.15 MPa) and a high tensile strain at break (575 ± 75%) (Figure S1b, Supporting Information). In addition, dynamic mechanical analysis (DMA, Figure 1b) and differential scanning calorimetry (DSC, Figure 1c) reveal a sharp modulus transition across T_m from 16 to 0.82 MPa. The quantitative shape-memory behaviors (Figure 1d) indicate near perfect shape fixing (99.9%) and recovery (99.4%), as well as excellent cyclic stability. The quantitative values of shape fixing (R_f) and shape recovery (R_r) were calculated from the shape-memory cycle (Figure 1d) by using the following equations

$$R_f = \varepsilon_d / \varepsilon_{dload} \tag{1}$$

and

$$R_r = (\varepsilon_d - \varepsilon_{rec}) / \varepsilon_d \tag{2}$$

where ε_{dload}, ε_d, and ε_{rec} represent the maximum strain under load, the fixed strain after cooling and load removal, and the recovered strain after heating, respectively. Figure 1e qualitatively demonstrates the shape-memory effect and the processability of SMPs of this type. Here, a laser-cut sample in a prescribed 2D geometry deforms into a 3D flower shape that is fixed by cooling below T_c. The original shape can be recovered by heating above T_m. Milk-white and transparent regions correspond to crystalline and amorphous states, respectively.

These SMPs can serve as platforms for remotely triggered formation of 3D mesostructures via compressive buckling-induced assembly (Figure 1f). The strategy starts by transfer of microfabricated 2D precursors consisting of almost any combination of thin-film materials and geometries onto a prestrained substrate of a bilayer of SMP (200 µm thick) and a soft silicone material (Dragon Skin 10, ≈20 µm thick). A patterned layer of silicon dioxide (SiO_2, 50 nm thick) selectively deposited onto certain regions of the 2D precursors defines locations of bonding sites to the substrate. Specifically, exposure to ultraviolet-induced ozone activates hydroxyl groups on these SiO_2 locations and the silicone surface of the substrate, allowing them to chemically bond upon contact.

A unique set of capabilities follows from incorporation of the SMP into the substrate. For example, the precursors can be maintained in their 2D geometry without application of external forces to stretch the substrate, simply by cooling the substrate below T_c (**Figure 2**a, stage I), where the SMP has a high modulus. In this state, the system can be deformed dramatically into desired configurations, including those that fit inside challenging operating environments (e.g., an ingestible gelatin capsule; Figure 2a, stage II). The 2D precursors then transform into 3D structures when the temperature rises above T_m, thereby inducing unfolding and shrinking of the SMP substrate back to its original geometry, in a remote and on-demand manner. Experimental demonstrations highlighted in Figure 2b–d include photolithographically defined 2D precursors of gold (20 nm thick) layers encapsulated by polyimide
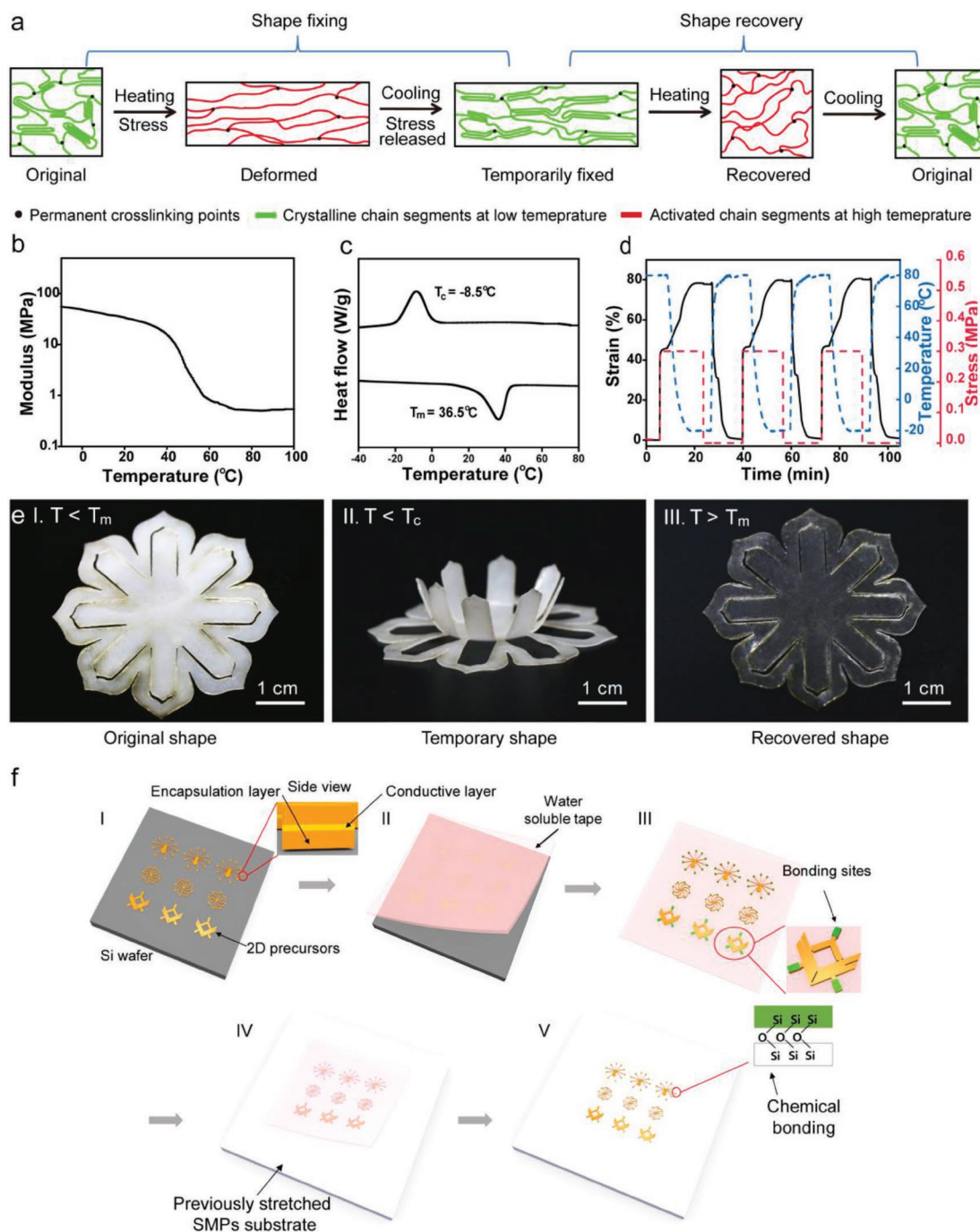
Figure 1. Thermomechanical characterization of the SMP and its application to compressive buckling-induced 3D assembly. a) Crystallization-enabled shape-memory mechanisms of the SMP. b) Dynamic mechanical analysis of the SMP reveals a glassy state modulus of ≈80 MPa at $T < T_m$, and a rubbery state modulus of 0.8 ± 0.1 MPa at $T > T_m$. c) Differential scanning calorimetry of the SMP indicates that $T_c = -8.5$ °C and $T_m = 36.5$ °C. d) Cyclic strain and recovery of the SMP at 80 °C with 99.9% shape fixity and 99.4% recovery. e) A demonstrative shape-memory cycle of the SMP from an original shape (left, $T < T_m$) to a temporary shape (mid, $T < T_c$) and to the recovered shape (right, $T > T_m$). f) Schematic illustration of a method to use the SMPs as a platform for compressive buckling-induced 3D assembly: I) fabricate 2D precursors on a silicon wafer, II) retrieve the 2D precursors using a water-soluble tape, III) deposit SiO_2 selectively on the 2D precursors, IV) transfer the 2D precursors onto a stretched SMP substrate, and V) remove the water-soluble tape.

(PI, 6 µm), transferred and bonded onto a prestretched SMP substrate (40% biaxially) and held by a mechanical stretcher (Figure 2b). Cooling below T_c allows release from the stretcher, and subsequent deformation into a cylindrical shape to fit into a gelatin capsule with an inner diameter of 8 mm. Alternatively, folding can transform the structure into a geometry one-sixth
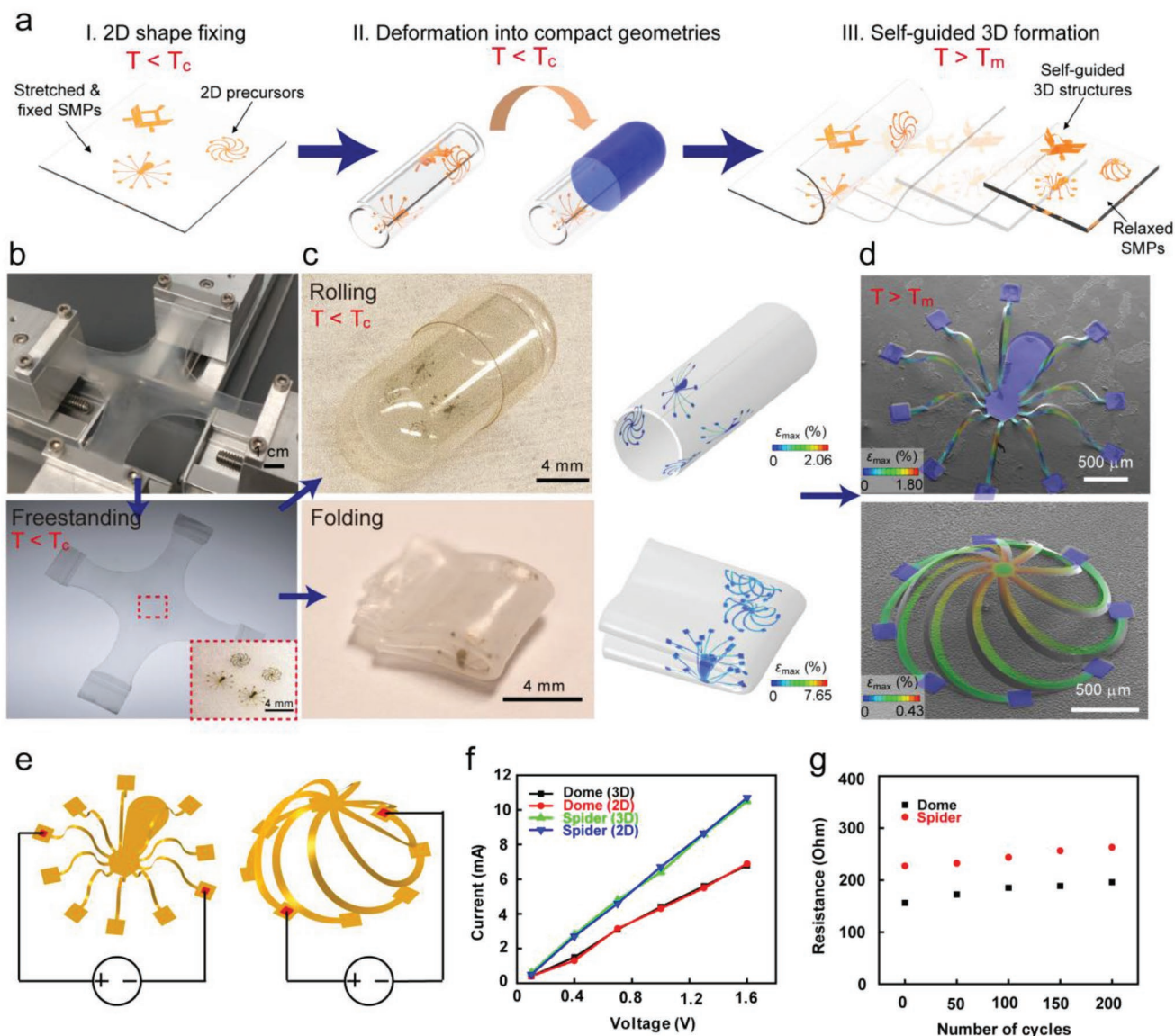
**ADVANCED
SCIENCE NEWS**

www.advancedsciencenews.com

**ADVANCED
MATERIALS**

www.advmat.de

Figure 2. Remote, on-demand, and self-guided formation of 3D mesostructures. a) Schematic illustration of the process: I) assembled 2D precursors on a stretched and shape-fixed SMP substrate, II) SMP substrate deformed into a compact geometry while maintaining the prestrain, and III) self-guided formation of a 3D mesostructure by remote heating. b) Optical images of (top) the previously stretched SMP substrate and (bottom) the assembled 2D precursors on the freestanding, shape-fixed SMP substrate. c) Optical images of the deformed SMP substrate with 2D precursors inside a gelatin capsule (top) or folded thrice (bottom), and FEA results showing the principal strain distributions in each deformed state. d) Scanning electron microscopy (SEM) images and overlapped FEA results showing quantitative geometric agreement, as well as principal strain distribution of the as-formed 3D structures: spider (top) and dome (bottom). e) Schematic illustration of spider (left) and dome (right) structures with highlighted electrical contact opening. f) I–V curves measured from Au conductive traces into the dome and spider structures before/after 3D formation. g) Resistance of the spider and dome structures as a function of the number of stretching/releasing cycles.

of its original size (Figure 2c). Placing these systems into a bath of warm water at a temperature greater than T_m triggers an unfolding and unrolling process, and an overall contraction of the SMP to its original shape within 5 s in warm water at 38 °C, leading to the formation of 3D structures (Figure 2d) in a manner that can be quantitatively captured by 3D finite-element analysis (FEA, Figure 2c,d). After 2D-to-3D transformation, the underlying substrate provides an additional degree of mechanical constraint to maintain the resulting 3D geometries regardless of the surrounding temperature. The SMPs do not

show signs of degradation when operated above T_m for weeks, provided that the temperature is not excessive (e.g., >200 °C). Despite dramatic deformations such as those shown in Figure 2c, the resulting 3D structures exhibit no defects (Figure 2d). Detailed fabrication procedures can be found in the Experimental Section. We demonstrate the high yield and throughput of this technique by fabricating a 3-by-3 array of mesostructures in a single batch, consisting of nine different geometries (Figure S2, Supporting Information). FEA results show quantitatively good agreement. For a number of arrays

**ADVANCED
SCIENCE NEWS**

www.advancedsciencenews.com

**ADVANCED
MATERIALS**

www.advmat.de

tested, the overall fabrication yield exceeds 96%, as defined by the number of structures that assemble into desired 3D shapes. We further demonstrate the miniaturization of this technique by fabricating 3D structures using the same procedures but with lateral dimensions of <400 µm (Figure S3, Supporting Information).

Measurements of resistance of the Au traces before and after 3D assembly verify the absence of changes in electrical properties associated with these various changes in shape. Figure 2e highlights the positions of electrodes for each structure for the measurements. Results in Figure 2f show that the current–voltage characteristics remain largely unchanged before and after 3D assembly, with corresponding average resistance values of 240 ± 15 and 153 ± 8 Ω for the spider- and dome-shaped structures, respectively. Tests of the robustness of the electrical connections verify that stretching/releasing the SMP substrates for up to 200 cycles induces neither significant increase in resistance (Figure 2g) nor noticeable cracks in the conductors under microscope inspection. The slight increases in resistance after 200 cycles are 25% for "dome" and 15% for "spider" structures, respectively, which can occur in stretchable electronic systems under these types of biaxial stretching conditions.[52–54] These results suggest applicability of these concepts in soft, stretchable microelectronic devices that can be deployed in compact geometries (e.g., delivery through the

human esophagus), and then transformed into complex, functional 3D layouts remotely (e.g., in the human stomach) by thermal triggering.

The highly stretchable SMP substrate and its responsiveness to both thermal and mechanical forms of actuation afford multiple degrees of control for advanced 3D assembly (**Figure 3**a), surpassing those reported previously that solely reply on mechanical actuations provided by the elastomeric substrates.[55,56] For example, thermomechanical actuation performed in a sequential order allows for programmable and individually addressable 3D assembly of a closely packed array of devices. The substrate in this case involves small islands of SMPs integrated into a large matrix of soft silicone (Figure 3b), formed through laser cutting and molding (see Figure S4 in the Supporting Information and the Experimental Section for details). To compensate for the modulus mismatch between the rubbery SMPs (0.82 MPa) and the silicone (0.17 MPa), the thickness ratio of the two can be modulated to achieve desired strain distributions for application of a given global strain to the heterogeneous substrate. Results of measured strains in the SMP islands and the silicone under a global strain of ≈50% for cases of different thickness ratios (Figures S5 and S6, Supporting Information), together with results of FEA, appear in Figure 3c. In this plot, the strain in the SMP and its thickness are normalized by the global strain and the thickness of
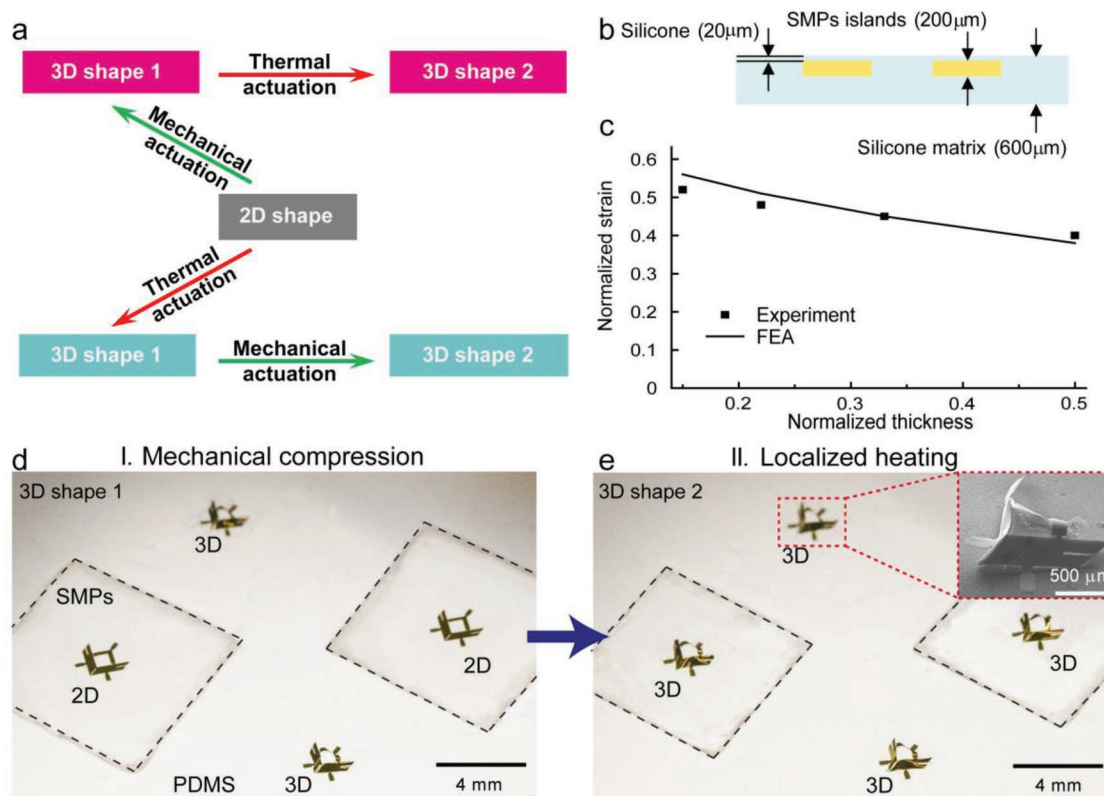

Figure 3. Advanced 3D structures with multiple degrees of control enabled by sequential actuation processes. a) Flow chart of the sequential actuation process. b) Schematic illustration of the cross section of the silicone/SMP substrate. c) Experimental results and FEA plot of the normalized strain in the substrate as a function of the normalized thickness of the samples. d) Optical image of the silicone/SMP substrate after selective mechanical actuation of 2D precursors on the silicone surface. e) Optical image of a silicone/SMP substrate after selective thermal actuation of 2D precursors on SMP islands.
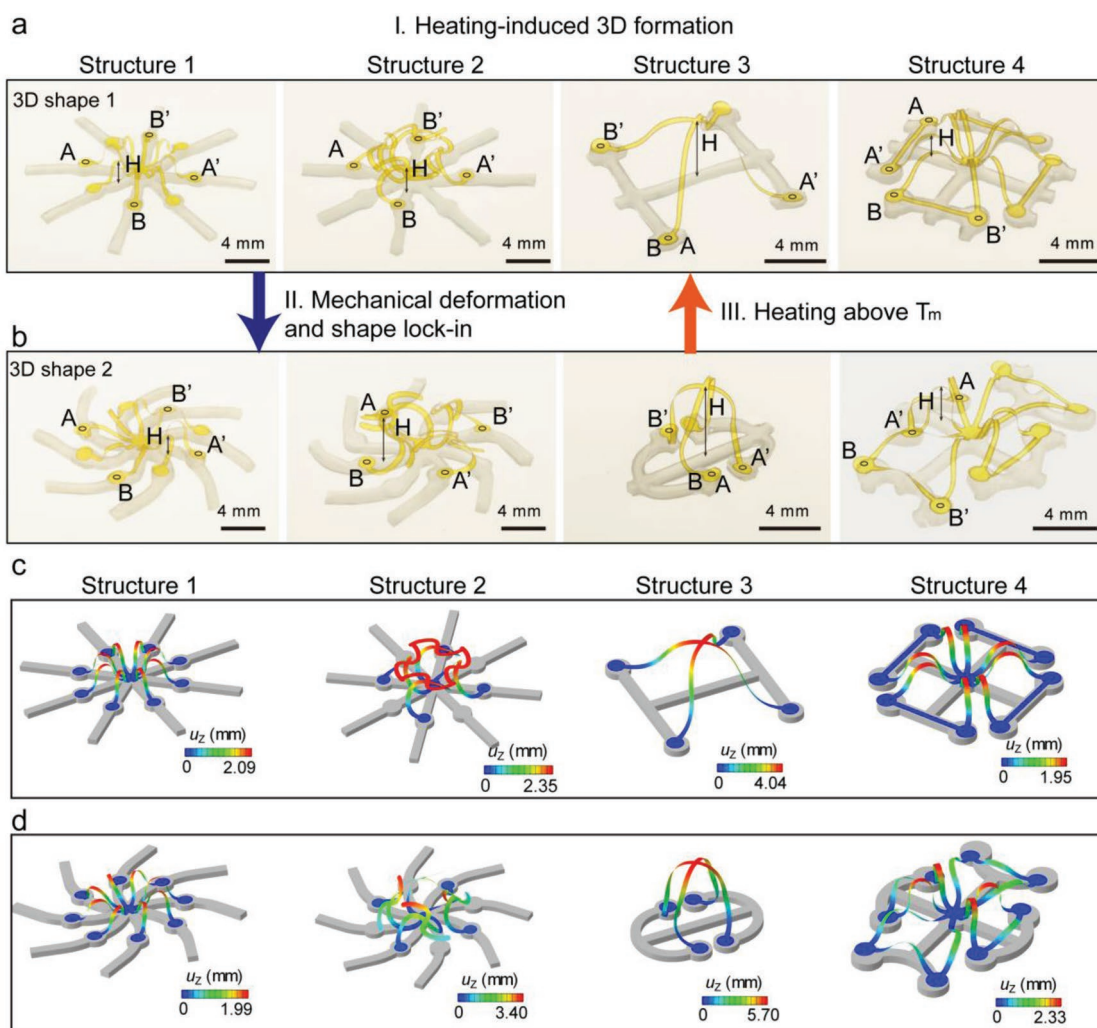
**ADVANCED
SCIENCE NEWS**

www.advancedsciencenews.com

**ADVANCED
MATERIALS**

www.advmat.de

Figure 4. Alternative route to sequential actuation processes by changing the order of the thermomechanical load. a) Optical images of the heating-induced 3D assembly of 2D precursors on SMP substrates in ribbon configurations. b) Optical images of the new 3D configurations induced by mechanical deformation and shape fixation. The length A–A′, B–B′, and height H for each structure before and after the shape change are provided in Table 1. c,d) FEA results for the structures in (a) and (b) showing quantitative geometric agreement, as well as z-axis deflection before and after shape change.

silicone matrix, respectively. The results show that the strain in the SMP increases as the thickness of silicone increases. Demonstrations of 3D assembly using this heterogeneous substrate involve first applying a 60% biaxial global strain to the substrate when the SMP is in its rubbery state, then bonding a 2-by-2 array of 2D precursors with two of the structures aligned to the SMP islands, and finally cooling the stretched substrate below T_c to fix the shape. Removing the external forces releases the strain in the portion of substrate that only has silicone, thereby transforming the corresponding 2D precursors into 3D structures that resemble birds, in a manner consistent with FEA (Figure S7, Supporting Information). The precursors on the SMP islands remain in their 2D shapes, as shown in Figure 3d. Localized heating can trigger the 2D-to-3D transformation on the SMP islands in a controlled manner (Figure 3e). The inset of Figure 3e shows the integrity of the resulting 3D structures after this programmed, thermally induced assembly.

Reversing the order of thermomechanical actuation allows for a second shape change in as-formed 3D structures, in ways that would be difficult to reproduce with previous methods. As shown in **Figure 4**a and Figure S8 (Supporting Information), a simple demonstration involves first selective attachment of 2D precursors onto prestrained, patterned SMP substrates in ribbon configurations, followed by transformation into 3D mesostructures by thermal actuation. Mechanically manipulating the SMP substrate induces a new 3D configuration at a temperature above T_m, in this case by fitting the substrate into a predesigned mold (Figure S9, Supporting Information). The new configuration can be fixed by cooling below T_c (Figure 4b). **Table 1** shows quantitative changes in dimensions of the 3D mesostructures before and after SMP-induced shape changes. FEA results that capture these effects are shown in Figure 4c,d. These additional options in 3D assembly have potential to extend to reversible operations by use of shape-memory alloys and composites.[40–42] Additional examples of a ring decorated

**ADVANCED
SCIENCE NEWS**

www.advancedsciencenews.com

**ADVANCED
MATERIALS**

www.advmat.de

Table 1. Dimensions of 3D mesostructures in Figure 4. The variation in the distance changes in dimensions between the specified bonding site and the height of the 3D mesostructures.

Characteristic dimension	Structure 1		Structure 2		Structure 3		Structure 4	
	Before	After	Before	After	Before	After	Before	After
A–A′ [mm]	9.7	8.7	9.7	8.5	9	2.2	9.2	5.8
B–B′ [mm]	9.7	8.7	9.7	8.6	9.9	5.4	9.2	12.8
H [mm]	2.3	2.2	2.3	3.3	3.8	5.4	2.0	2.4

with an array of flower-like 3D mesostructures are shown in Figure S10 (Supporting Information).

A simple application of these ideas involves the design and fabrication a mobile, aquatic robot that can switch modes of motion by remote thermal stimuli (**Figure 5**a; Figure S11, Supporting Information). Here, a thin layer of platinum (Pt, 100 nm thick) deposited and patterned onto PI (6 µm thick) acts as a catalyst for the decomposition reaction of hydrogen peroxide into water and oxygen. The generated oxygen bubbles drive motion of the robot in a tank of hydrogen peroxide (30% H_2O_2 in H_2O by weight). Coupled with an SMP substrate laser-cut into the shape of a gripper, the robot, which is sufficiently

small to fit inside a gelatin capsule with an inner diameter of 5 mm (Figure 5b), can carry small cargo objects (polystyrene spheres, 1.5 mm in diameter). In mode 1, the oxygen bubbles form in a single direction perpendicular to the Pt layer, leading to a straight trajectory with an average speed of 1.1 mm s^{-1} (Figure 5d). By heating the SMP substrate above T_m, the 2D Pt layer transforms into a 3D turbine geometry via a process of unfolding and contracting of the SMP (Figure 5c). In this new shape, oxygen generation occurs in a multidirectional fashion to induce a circular mode of motion with an average speed of 1.6 mm s^{-1} (Figure 5d). Trajectories computed by FEA (overlaid in Figure 5d) show good agreement with the experimental
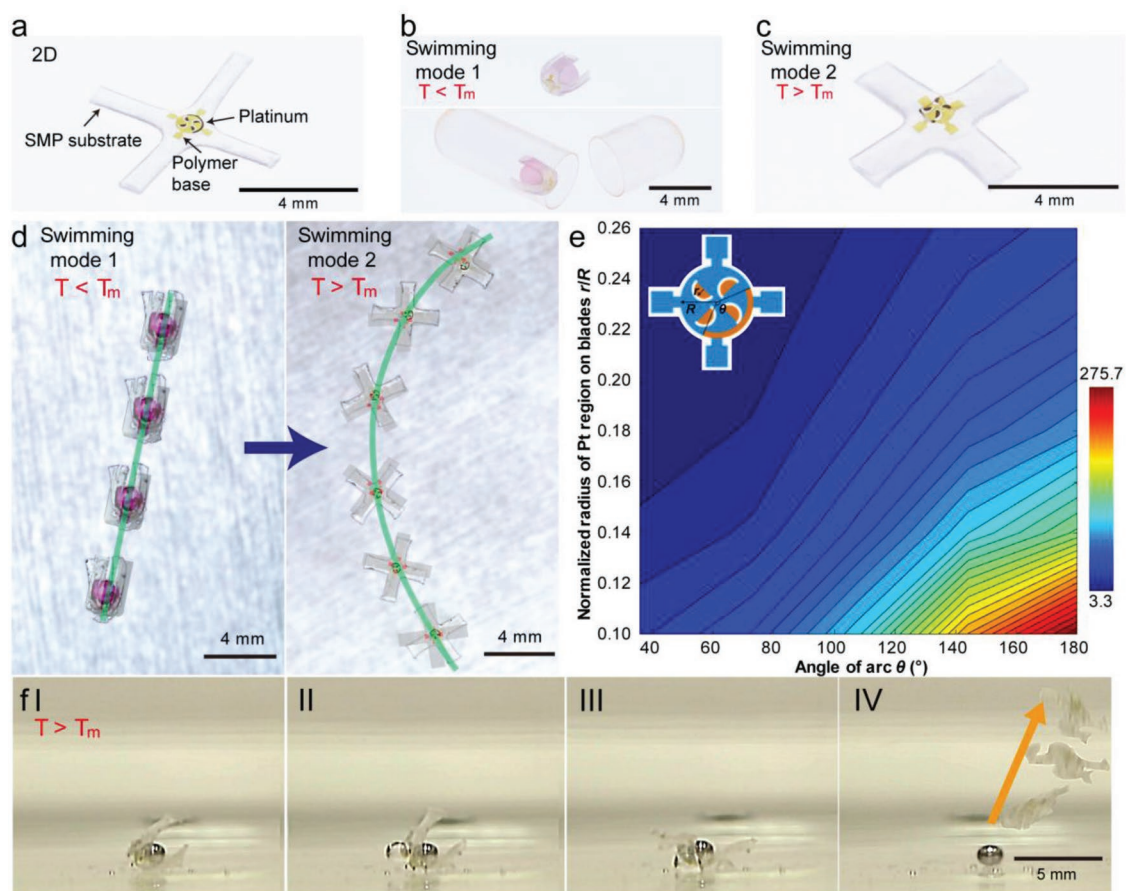

Figure 5. Aquatic robots with switchable modes of motion. a) Optical image of a 2D precursor and stretched SMP substrate. b) Optical images of a robot in mode 1, gripping a sphere. c) Optical image of a robot in mode 2 after shape recovery. d) Superimposed experimental and numerical results of the motion trajectory in (left) mode 1 and (right) mode 2. e) FEA study of the relationship between robot dimension and mode of motion. The contour plot shows the normalized radius of motion trajectory of the robot as a function of the normalized radius of the Pt patterns and the angle of the Pt arc. f) Sequential optical images showing shape recovery of the robot in hydrogen peroxide solution.

results. Opening of the gripper configuration also results in release of the small objects. The detailed motions can be found in Movies S1 and S2 (Supporting Information).

The radius of curvature of the circular mode can be tuned by tailoring the geometry of the Pt layer. Examples to illustrate the effects include a peripheral arc-shaped stripe and four semicircular turbine blades (Figure 5e, inset). The stripe controls the degree of linear motion, while the blades dominate the rotational motion. In combination, these patterns enable motions in an approximately circular trajectory, with a radius that can be controlled by adjusting the contribution from the linear/rotational motion (through tailoring patterns of Pt stripe and blades). Figure 5e highlights the radius of curvature (normalized by R, the overall radius of the circular shape in the 2D precursor) of the circular trajectory, illustrating its dependence on the geometries of the blades (radius r, normalized by R) and the stripe (angle of arc θ). The contour plot denotes the normalized curvature radius ranging from 3.3 to 275.7 (corresponding to a range between 1.65 and 137.83 mm in curvature radius) as predicted by simulation. Longer stripes (for $\theta \leq 180°$) and smaller blades give rise to trajectories that map out larger circles.

With stainless-steel spheres (1.5 mm in diameter, $\rho = 8000$ kg m^{-3}) as cargo, the structure loses its buoyancy and sinks rapidly to the bottom of the tank. Upon application of a thermal trigger, the robot releases the sphere (Figure 5f), resulting in a resurfacing that allows motion to continue in mode 2 (Movie S3, Supporting Information). Such cargo objects can also be used for additional control over the motion, e.g., via external magnetic fields for ferromagnetic objects (Figure S12 and Movie S4, Supporting Information). Finally, the fabrication and assembly processes enable integration of microelectronic components, e.g., light-emitting diodes (LEDs) and temperature sensors (Figures S13 and S14, Supporting Information), due to the compatibility of the overall approach with established planar and thin-film processing methods.

In conclusion, this paper introduces options in remote, triggered assembly of 3D mesostructures enabled by highly stretchable, semicrystalline SMPs with thermally induced shape transitions near body temperature. The processability of the SMPs (molding and laser cutting), together with capabilities for fabricating microscale 2D precursors by conventional planar techniques (photolithography and laser cutting), creates a variety of design opportunities, with potential applications 3D microelectronics, microrobotics, biomedical devices, and other areas. Integrating advanced sensors and actuators using established 2D schemes and thin-film deposition/patterning techniques and exploiting advanced shape-memory materials for reversible shape changes represent promising directions for future work.

Experimental Section

Materials and Fabrication of SMP Films: PCL ($M_n = 2000$, Sigma–Aldrich), HDI (Sigma–Aldrich), PHDI (Sigma–Aldrich), and tin(II) acetate (catalyst, TCI) were all used as received.

PCL (2 g) was weighed into a glass bottle and dissolved in butyl acetate. Afterward, stoichiometric amounts of HDI and PHDI (mole ratio, HDI:PHDI = 1:1) and catalyst (0.5 wt%) were added into the bottle. The mixture was poured into an aluminum pan and curing was conducted at 60 °C for 2 h. Finally, the sample was vacuum-dried overnight and demolded.

Thermal and Mechanical Characterizations of SMPs: DSC (TA Q200) was performed with a cooling and heating rate of 10 °C min^{-1}. DMA (TA Q500) was conducted at 1 Hz, 0.2% strain, and a heating rate of 3 °C min^{-1}.

The tensile modulus was determined with a universal material testing machine (Zwick/Roell Z005) at 70 °C and a tensile speed of 5 mm min^{-1}. All samples were tested in dog bone shapes with the neck dimension of 0.8×2.5 mm^2. At least five specimens were tested for each case.

Characterization of the Shape-Memory Effect: Quantitative measurements of shape-memory cycles were conducted with the same DMA machine under stress-controlled condition. For qualitative shape-memory characterization, the sample was first heated above T_m and then deformed under external force followed by cooling below T_c. After releasing the force, a temporary shape was fixed. The shape recovery step was accomplished by heating under a stress-free condition.

Fabrication of SMP Substrates: SMP films were cut into the desired substrate designs using a CO$_2$ laser cutter (Epilog Fusion M2 32, EpilogLaser), followed by rinsing with isopropyl alcohol (IPA), deionized (DI) water, and blowing dry with compressed nitrogen to remove any residue. A silicone precursor (Dragon Skin 10, Smooth-On) was then spin-coated on the SMP films at 3000 rpm for 30 s and cured at room conditions for 24 h.

SMPs/silicon composite substrates shown in Figure 3b were prepared by laser cutting 200 μm thick SMP films into 1 by 1 cm^2 squares and placing them at desired locations of a 140 mm diameter Petri dish (Figure S4, Supporting Information). Here the SMP films were adhered onto the Petri dish by heating them above T_m and applying gentle pressure. Maintaining the pressure and cooling below T_c created strong adhesion between the Petri dish and the SMP films. Next, selected amounts (6, 9, 14, and 20 mL) of silicone precursor for controlled thicknesses (0.4, 0.6, 0.9, and 1.3 mm) were spin-cast on top at 500 rpm for 20 s until the material just reached the sidewalls of the Petri dish. Silicone was then cured under room conditions for 24 h and peeled from the Petri dish together with the SMP. The composite substrate was flipped, and the other side was spin-cast with silicone at 3000 rpm for 30 s to yield a thin layer of silicone (≈20 μm) on the SMP islands.

Fabrication of 2D Precursors and Transformation into 3D Mesostructures: Fabrication of 2D precursors began with rinsing a silicon wafer with acetone, IPA, and DI water followed by drying under a stream of nitrogen. Poly(methyl methacrylate) (PMMA A7, Microchem) was spin-cast on the silicon wafer at 3500 rpm for 40 s and baked at 180 °C for 3.5 min. A polyimide precursor (PI-2545, Dupont) was spin-cast on the PMMA layer at 2000 rpm for 60 s and cured at 250 °C in a vacuum oven. Repeating this process twice yielded a 6 μm thick PI layer with good thickness uniformity. A conductive layer of Cr (5 nm)/Au (20 nm) was deposited by electron-beam evaporation (FC-2000, Temescal) onto the PI layer and wet etched through a mask of photoresist (AZ5214, Microchem). Using the conductive layer as an etch mask, the PI and PMMA layers were dry-etched simultaneously using an O$_2$ plasma at 20 sccm, 200 W, 50 mTorr for 20 min. Then the sample was immersed in an acetone bath for 24 h to remove the PMMA sacrificial layer and release the 2D precursors from the wafer. The 2D precursors were then retrieved using a water-soluble tape (Aquasol) and aligned with a separately prepared Kapton film mask (25 μm) to only expose the bonding sites. Layers of Ti (5 nm)/SiO$_2$ (50 nm) were then deposited by electron-beam evaporation onto the sample.

After removing the Kapton film, the 2D precursors and the separately prepared SMP substrates, previously prestrained using a mechanical stretcher, were exposed to ultraviolet-induced ozone (UVO-Cleaner, Jelight) and laminated together with slight pressure. After heating in a convection oven at 70 °C for 7 min, the SMP substrate (while still stretched by the stretcher) was cooled below T_c in a refrigerator to fix the shape. The water-soluble tape was then removed with water. Detaching the SMP substrate from the stretcher and heating above T_m completed the 2D-to-3D assembly process.

Fabrication of 3D Aquatic Robots: The process began with fabrication of 2D precursors using procedures described previously to yield a 6 μm

thick layer of PI on the PMMA layer. Cr (8 nm)/Pt (100 nm) was then deposited onto the PI layer by sputtering (ATC Orion 8 HV sputtering system, AJA). Etching of the Pt used hot aqua regia solution (volume ratio, HCl:HNO$_3$ = 3:1) at 60 °C for 40 s with photoresist as a masking layer. The Cr layer was successively patterned with another photoresist mask to yield a hard mask for dry etching of the PI and PMMA with an O$_2$ plasma at 20 sccm, 200 W, 50 mTorr for 20 min. The Cr was then removed using a chromium etchant (Transene). Immersed in acetone for 24 h removed the PMMA layer to allow retrieval of the 2D precursors onto a water-soluble tape. A silicone adhesive (Clear Sealant, Dow corning) was carefully applied onto the bonding sites of the 2D precursors through a Kapton mask. The 2D precursors were then aligned and laminated onto a SMP substrate stretched to 30% biaxially, and held in this position for 1 h under room conditions to cure the silicone glue for selective bonding. Removing the water-soluble tape with water and mechanically deforming the substrate into a gripper geometry assembled the 2D precursors into 3D robot mode 1.

Finite Element Analysis: 3D FEA used the commercial software package Abaqus to analyze the nonlinear deformation of substrates and to predict the postbuckling behavior of 2D precursor structures under compressive forces induced by the prestretched substrates. Linear buckling analyses for the 2D precursor structures under compression were executed to determine the critical buckling strain and corresponding buckling mode, which were then considered as initial geometric imperfections in postbuckling computations. Deformed shapes and strain distributions at different prestrains for the 2D precursor structures can then be obtained. Eight-node solid elements and four-node shell elements were used for the substrates and the 2D precursor structures, respectively. The convergence test of the mesh size was performed to ensure accuracy. The substrate material (Dragon Skin 10 Slow) was modeled as an incompressible Mooney–Rivlin solid, with an elastic modulus of $E_{DragonSkin} = 166$ kPa. For the SMPs, a multibranch viscoelastic model[41] was implemented to capture the thermo-viscoelastic and shape-memory behaviors. The PI was simulated as a linear elastic solid with an elastic modulus of $E_{PI} = 2.5$ GPa and a Poisson's ratio of $\nu_{PI} = 0.34$. Metal materials, such as Au and pt, have elastoplastic material behavior. An idealized elastoplastic model (without hardening) was used in FEA, and the yield strain was chosen as 0.3%. The elastic modulus and Poisson's ratio were $E_{Au} = 78$ GPa and $\nu_{Au} = 0.44$ for Au, and $E_{Pt} = 168$ GPa and $\nu_{Pt} = 0.38$ for Pt.

Multibody Dynamics Analysis: Multibody dynamics simulations were conducted in the commercial software COMSOL Multiphysics to analyze the motions of 3D aquatic robot in Figure 5. The 3D geometries, predicted from the postbuckling analysis in Abaqus, were imported into COMSOL multibody dynamics module. A time-dependent solver was chosen for the motion analysis. The driving forces due to the generation of oxygen bubbles were modeled as uniform pressure applied on the Pt-patterned regions. The resistance from the fluids was simplified as nodal forces with magnitude proportional to and direction opposite to the local velocity. Linear hexahedral elements were used to mesh the robot.

Supporting Information

Supporting Information is available from the Wiley Online Library or from the author.

Acknowledgements

Conflict of Interest

The authors declare no conflict of interest.

Keywords

[1] X. Li, J. Cai, X. Lu, Y. Shi, D. Gong, D. Su, D. Zhang, *J. Mater. Chem. C* **2018**, *6*, 4191.

[2] J. J. Adams, E. B. Duoss, T. F. Malkowski, M. J. Motala, B. Y. Ahn, R. G. Nuzzo, J. T. Bernhard, J. A. Lewis, *Adv. Mater.* **2011**, *23*, 1335.

[3] X. Wang, X. Guo, J. Ye, N. Zheng, P. Kohli, D. Choi, Y. Zhang, Z. Xie, Q. Zhang, H. Luan, K. Nan, B. H. Kim, Y. Xu, X. Shan, W. Bai, R. Sun, Z. Wang, H. Jang, F. Zhang, Y. Ma, Z. Xu, X. Feng, T. Xie, Y. Huang, Y. Zhang, J. A. Rogers, *Adv. Mater.* **2019**, *31*, 1805615.

[4] H. Fu, K. Nan, W. Bai, W. Huang, K. Bai, L. Lu, C. Zhou, Y. Liu, F. Liu, J. Wang, M. Han, Z. Yan, H. Luan, Y. Zhang, Y. Zhang, J. Zhao, M. Li, J. W. Lee, Y. Liu, D. Fang, X. Li, Y. Huang, Y. Zhang, J. A. Rogers, *Nat. Mater.* **2018**, *17*, 268.

[5] F. Liu, Y. Chen, H. Song, F. Zhang, Z. Fan, Y. Liu, X. Feng, J. A. Rogers, Y. Huang, Y. Zhang, *Small* **2019**, *15*, 1804055.

[6] W. Lee, Y. Liu, Y. Lee, B. K. Sharma, S. M. Shinde, S. D. Kim, K. Nan, Z. Yan, M. Ham, Y. Huang, Y. Zhang, J. H. Ahn, J. A. Rogers, *Nat. Commun.* **2018**, *9*, 1417.

[7] D. D. Karnaushenko, D. Karnaushenko, H.-J. Grafe, V. Kataev, B. Buchner, O. G. Schmidt, *Adv. Electron. Mater.* **2018**, *4*, 1800298.

[8] E. Diller, M. Sitti, *Adv. Funct. Mater.* **2014**, *24*, 4397.

[9] S. Lee, S. Lee, S. Kim, C. H. Yoon, H. J. Park, J. Y. Kim, H. Choi, *Sci. Rep.* **2018**, *8*, 3691.

[10] A. Laskar, O. E. Shklyaev, A. C. Balazs, *Sci. Adv.* **2018**, *4*, eaav1745.

[11] K. Nan, H. Wang, X. Ning, K. A. Miller, C. Wei, Y. Liu, H. Li, Y. Xue, Z. Xie, H. Luan, Y. Zhang, Y. Huang, J. A. Rogers, P. V. Braun, *ACS Nano* **2019**, *13*, 449.

[12] K. Nan, S. D. Kang, K. Li, K. J. Yu, F. Zhu, J. Wang, A. C. Dunn, C. Zhou, Z. Xie, M. T. Agne, H. Wang, H. Luan, Y. Zhang, Y. Huang, G. J. Snyder, J. A. Rogers. *Sci. Adv.* **2018**, *4*, eaau5849.

[13] X. Wang, S. Niu, Y. Yin, F. Yi, Z. You, Z. L. Wang, *Adv. Energy Mater.* **2015**, *5*, 1501467.

[14] Y. Hu, J. Yang, Q. Jing, S. Niu, W. Wu, Z. L. Wang, *ACS Nano* **2013**, *7*, 10424.

[15] M. Han, H. Wang, Y. Yang, C. Liang, W. Bai, Z. Yan, H. Li, Y. Xue, X. Wang, B. Akar, H. Zhao, H. Luan, J. Lim, I. Kandela, G. A. Ameer, Y. Zhang, Y. Huang, J. A. Rogers, *Nat. Electron.* **2019**, *2*, 26.

[16] T. G. Leong, C. L. Randall, B. R. Benson, N. Bassik, G. M. Stern, D. H. Gracias, *Proc. Natl. Acad. Sci. USA* **2009**, *106*, 703.

[17] R. Feiner, L. Engel, S. Fleischer, M. Malki, I. Gal, A. Shapira, Y. Shacham-Diamand, T. Dvir, *Nat. Mater.* **2016**, *15*, 679.

[18] K. I. Jang, K. Li, H. U. Chung, S. Xu, H. N. Jung, Y. Yang, J. W. Kwak, H. H. Jung, J. Song, C. Yang, A. Wang, Z. Liu, J. Y. Lee, B. H. Kim, J. H. Kim, J. Lee, Y. Yu, B. J. Kim, H. Jang, K. J. Yu, J. Kim, J. W. Lee, J. W. Jeong, Y. M. Song, Y. Huang, Y. Zhang, J. A. Rogers, *Nat. Commun.* **2017**, *8*, 15894.

[19] S. Tasoglu, E. Diller, S. Guven, M. Sitti, U. Demirci, *Nat. Commun.* **2014**, *5*, 3124.

[20] M. Zarek, M. Layani, I. Copperstein, E. Sachyani, D. Cohn, S. Magdassi, *Adv. Mater.* **2016**, *28*, 4449.

[21] D. Mousanezhad, S. Babaee, H. Ebrahimi, R. Ghosh, A. S. Hamouda, K. Bertoldi, A. Vaziri, *Sci. Rep.* **2016**, *5*, 18306.

[22] C. Ladd, J. H. So, J. Muth, M. D. Dickey, *Adv. Mater.* **2013**, *25*, 5081.

[23] J. L. Shi, C. Tang, H. J. Peng, L. Zhu, X. B. Cheng, J. Q. Huang, W. Zhu, Q. Zhang, *Small* **2015**, *11*, 5243.

[24] J. C. Yoon, J. S. Lee, S. I. Kim, K. H. Kim, J. H. Jang, *Sci. Rep.* **2013**, *3*, 1788.

[25] B. H. Min, D. W. Kim, Y. H. Kim, H. O. Choi, S. W. Jang, H. T. Jung, *Carbon* **2014**, *80*, 446.

[26] M. Y. B. Zion, X. He, C. C. Maass, R. Sha, N. C. Seeman, P. M. Chaikin, *Science* **2017**, *358*, 633.

[27] V. N. Manoharan, *Science* **2015**, *349*, 1253751.

[28] D. J. Kraft, R. Ni, F. Smallenburg, M. Hermes, K. Yoon, D. A. Weitz, A. van Blaaderen, J. Groenewold, M. Dijkstra, W. K. Kegel, *Proc. Natl. Acad. Sci. USA* **2012**, *109*, 10787.

[29] W. Xu, Z. Qin, C. T. Chen, H. R. Kwag, Q. Ma, A. Sarkar, M. J. Buehler, D. H. Gracias, *Sci. Adv.* **2017**, *3*, e1701084.

[30] Q. Liu, B. Xu, *Soft Matter* **2018**, *14*, 5968.

[31] Z. Tian, L. Zhang, Y. Fang, B. Xu, S. Tang, N. Hu, Z. An, Z. Chen, Y. Mei, *Adv. Mater.* **2017**, *29*, 1604572.

[32] X. Cheng, Y. Zhang, *Adv. Mater.* **2019**, *31*, 1901895.

[33] Y. Zhang, F. Zhang, Z. Yan, Q. Ma, X. Li, Y. Huang, J. A. Rogers, *Nat. Rev. Mater.* **2017**, *2*, 17019.

[34] T. G. Leong, A. M. Zarafshar, D. H. Gracias, *Small* **2010**, *6*, 792.

[35] V. A. B. Quiñones, H. Zhu, A. A. Solovev, Y. Mei, D. H. Gracias, *Adv. Biosyst.* **2018**, *2*, 1800230.

[36] G. Huang, Y. Mei, *Small* **2018**, *14*, 17703665.

[37] D. Karnaushenko, T. Kong, O. G. Schmidt, *Adv. Mater. Technol.* **2019**, *4*, 1800692.

[38] Y. Zhang, Z. Yan, K. Nan, D. Xiao, Y. Liu, H. Luan, H. Fu, X. Wang, Q. Yang, J. Wang, W. Ren, H. Si, F. Liu, L. Yang, H. Li, J. Wang, X. Guo, H. Luo, L. Wang, Y. Huang, J. A. Rogers, *Proc. Natl. Acad. Sci. USA* **2015**, *112*, 11757.

[39] Z. Fan, K. C. Hwang, J. A. Rogers, Y. Huang, Y. Zhang, *J. Mech. Phys. Solids* **2018**, *111*, 215.

[40] Z. Wu, L. Li, Y. Yang, P. Hu, Y. Li, S. Y. Yang, L. V. Wang, W. Gao, *Sci. Rob.* **2019**, *4*, eaax0613.

[41] Q. Zhao, H. J. Qi, T. Xie, *Prog. Polym. Sci.* **2015**, *49–50*, 79.

[42] M. Behl, K. Kratz, J. Zotzmann, U. Nöchel, A. Lendlein, *Adv. Mater.* **2013**, *25*, 4466.

[43] Y. Bellouaard, *Mater. Sci. Eng., A* **2008**, *481–482*, 582.

[44] A. Irzhak, V. S. Kalashnikov, V. V. Kledov, D. S. Kuchin, G. A. Lebedev, P. V. Lega, N. A. Pikhtin, I. S. Tarasov, V. G. Shavrov, A. V. Shelyakov, *Tech. Phys. Lett.* **2010**, *36*, 329.

[45] Y. Yang, W. Gao, *Nat. Electron.* **2018**, *1*, 580.

[46] M. Lee, H. J. Shim, C. Choi, D. H. Kim, *Nano Lett.* **2019**, *19*, 2741.

[47] Y. Lee, J. Kim, B. Jang, S. Kim, B. K. Sharma, J. H. Kim, J. H. Ahn, *Nano Energy* **2019**, *62*, 259.

[48] H. Shin, B. k. Sharma, S. W. Lee, J. B. Lee, M. Choi, L. Hu, C. Park, J. H. Choi, T. W. Kim, J. H. Ahn, *ACS Appl. Mater. Interfaces* **2019**, *11*, 14222.

[49] H. Xu, C. Yu, S. Wang, V. Malyarchuk, T. Xie, J. A. Rogers, *Adv. Funct. Mater.* **2013**, *23*, 3299.

[50] J. Reeder, M. Kaltenbrunner, T. Ware, D. Arreaga-Salas, A. Avendano-Bolivar, T. Yokata, Y. Inoue, M. Sekino, W. Voit, T. Sekitani, T. Someya, *Adv. Mater.* **2014**, *26*, 4967.

[51] Z. Yu, Q. Zhang, L. Li, Q. Chen, X. Niu, J. Liu, Q. Pei, *Adv. Mater.* **2011**, *23*, 664.

[52] N. Liu, A. Chortos, T. Lei, L. Jin, T. R. Kim, W. G. Bae, C. Zhu, S. Wang, R. Pfattner, X. Chen, R. Sinclair, Z. Bao, *Sci. Adv.* **2017**, *3*, e1700159.

[53] K. Kim, J. Kim, B. G. Hyun, S. Ji, S. Y. Kim, S. Kim, B. W. An, J. U. Park, *Nanoscale* **2015**, *7*, 14577.

[54] C. F. Li, W. Li, H. Zhang, J. Jiu, Y. Yang, L. Li, Y. Gao, Z. Q. Liu, K. Suganuma, *ACS Appl. Mater. Interfaces* **2019**, *11*, 3231.

[55] K. Nan, H. Luan, Z. Yan, X. Ning, Y. Wang, A. Wang, J. Wang, M. Han, M. Chang, K. Li, Y. Zhang, W. Huang, Y. Xue, Y. Huang, Y. Zhang, J. A. Rogers, *Adv. Funct. Mater.* **2017**, *27*, 1604281.

[56] H. Luan, X. Cheng, A. Wang, S. Zhao, K. Bai, H. Wang, W. Pang, Z. Xie, K. Li, F. Zhang, Y. Xue, Y. Huang, Y. Zhang, *ACS Appl. Mater. Interfaces* **2019**, *11*, 3482.